Ancient MAPK ERK7 is regulated by an unusual inhibitory scaffold required for *Toxoplasma* apical complex biogenesis

Peter S. Back[a,1], William J. O'Shaughnessy[b,1], Andy S. Moon[c], Pravin S. Dewangan[b], Xiaoyu Hu[b], Jihui Sha[d], James A. Wohlschlegel[d], Peter J. Bradley[a,c,2], and Michael L. Reese[b,e,2]

[a]Molecular Biology Institute, University of California, Los Angeles, CA 90095; [b]Department of Pharmacology, University of Texas Southwestern Medical Center, Dallas, TX 75390; [c]Department of Molecular Microbiology and Immunology, University of California, Los Angeles, CA 90095; [d]Department of Biological Chemistry, David Geffen School of Medicine, University of California, Los Angeles, CA 90095; and [e]Department of Biochemistry, University of Texas Southwestern Medical Center, Dallas, TX 75390

Edited by Stephen M. Beverley, Washington University School of Medicine in St. Louis, St. Louis, MO, and approved April 16, 2020 (received for review December 6, 2019)

Apicomplexan parasites use a specialized cilium structure called the apical complex to organize their secretory organelles and invasion machinery. The apical complex is integrally associated with both the parasite plasma membrane and an intermediate filament cytoskeleton called the inner-membrane complex (IMC). While the apical complex is essential to the parasitic lifestyle, little is known about the regulation of apical complex biogenesis. Here, we identify AC9 (apical cap protein 9), a largely intrinsically disordered component of the *Toxoplasma gondii* IMC, as essential for apical complex development, and therefore for host cell invasion and egress. Parasites lacking AC9 fail to successfully assemble the tubulin-rich core of their apical complex, called the conoid. We use proximity biotinylation to identify the AC9 interaction network, which includes the kinase extracellular signal-regulated kinase 7 (ERK7). Like AC9, ERK7 is required for apical complex biogenesis. We demonstrate that AC9 directly binds ERK7 through a conserved C-terminal motif and that this interaction is essential for ERK7 localization and function at the apical cap. The crystal structure of the ERK7–AC9 complex reveals that AC9 is not only a scaffold but also inhibits ERK7 through an unusual set of contacts that displaces nucleotide from the kinase active site. ERK7 is an ancient and autoactivating member of the mitogen-activated kinase (MAPK) family and its regulation is poorly understood in all organisms. We propose that AC9 dually regulates ERK7 by scaffolding and concentrating it at its site of action while maintaining it in an "off" state until the specific binding of a true substrate.

kinase | scaffold | intrinsically disordered protein | cilium

Cilia are ancient eukaryotic organelles that organize signal-transduction cascades and mediate cell motility. These functions are driven by the cooperation of cytoskeleton and membrane structures and require specialized signaling and trafficking machinery for their biogenesis and maintenance (1–3). In apicomplexan parasites, the cilium is thought to have evolved to form the "apical complex" (4–7), which organizes the parasites' invasion machinery and for which the phylum is named. Apicomplexa include the causative agents of malaria, toxoplasmosis, and cryptosporidiosis, which all invade mammalian cells to cause disease. Like more typical eukaryotic cilia, the apical complex is composed of specialized microtubule structures inserted into the plasma membrane (8). In addition, the apical complex is the site of secretion of specialized organelles called micronemes and rhoptries that mediate the parasites' attachment to and invasion of host cells. In the asexual stage of most apicomplexans, secretion is thought to occur through a tubulin-rich structure in the apical complex called the conoid (8, 9). The apical complex is also intimately associated with an intermediate filament cytoskeleton called the inner-membrane complex (IMC) that scaffolds the apicomplexan cell, ensuring its correct morphology. The IMC anchors the parasite actin-based motility machinery (10), powering the parasite's motility as it glides across and invades host cells. While the IMC extends the length of the parasite, it has clearly segregated apical, medial, and basal subdomains that are defined by specific protein localization (11, 12). In *Toxoplasma gondii*, the IMC "apical cap" comprises the anterior-most ∼1 μm of the IMC, just basal to the apical complex. The apical cap appears to be a site at which actin regulators (13) and subcomponents of the parasite invasion machinery concentrate (14). While a number of IMC proteins have been genetically manipulated and evaluated phenotypically, their biochemical functions have been understudied.

In the present work, we identify one component of the *T. gondii* apical IMC, apical cap protein 9 (AC9), as essential to the parasite lytic cycle. We found that loss of AC9 results in parasites that are entirely unable to egress from their host cells or invade new cells. These deficiencies are attributable to the failure of the

Significance

Apicomplexan parasites include organisms that cause widespread and devastating human diseases such as malaria, cryptosporidiosis, and toxoplasmosis. These parasites are named for a structure, called the "apical complex," that organizes their invasion and secretory machinery. We found that two proteins, apical cap protein 9 (AC9) and an enzyme called ERK7, work together to facilitate apical complex assembly. Intriguingly, ERK7 is an ancient molecule that is found throughout Eukaryota, though its regulation and function are poorly understood. AC9 is a scaffold that concentrates ERK7 at the base of the developing apical complex. In addition, AC9 binding likely confers substrate selectivity upon ERK7. This simple competitive regulatory model may be a powerful but largely overlooked mechanism throughout biology.

Author contributions: P.S.B., W.J.O., A.S.M., P.S.D., X.H., P.J.B., and M.L.R. designed research; P.S.B., W.J.O., A.S.M., P.S.D., X.H., and J.S. performed research; P.S.B., W.J.O., P.S.D., X.H., J.S., J.A.W., P.J.B., and M.L.R. analyzed data; and P.S.B., W.J.O., P.S.D., P.J.B., and M.L.R. wrote the paper.

The authors declare no competing interest.

This article is a PNAS Direct Submission.

Data deposition: The crystal structure of the ERK7–AC9 complex reported in this paper has been deposited in the Protein Data Bank, https://www.pdb.org (PDB ID code 6V6A).

[1]P.S.B. and W.J.O. contributed equally to this work.

[2]To whom correspondence may be addressed. Email: pbradley@ucla.edu or michael.reese@utsouthwestern.edu.

This article contains supporting information online at https://www.pnas.org/lookup/suppl/doi:10.1073/pnas.1921245117/-/DCSupplemental.

First published May 14, 2020.

parasites to form a functional apical complex, as the conoids are entirely missing in mature parasites and regulated secretion is disrupted. These data provide insight into the functions of the IMC apical cap in regulating parasite development. Using proximity biotinylation, we defined the AC9 interaction network, which includes extracellular signal-regulated kinase 7 (ERK7), a conserved mitogen-activated protein kinase (MAPK) that regulates ciliogenesis in Metazoa (15, 16), and which we have recently shown is required for conoid formation (17). We demonstrated that AC9 is required for the correct localization of ERK7 at the apical cap, and that this scaffolding interaction is essential for apical complex maturation. Finally, we solved the crystal structure of the ERK7–AC9 complex, which revealed that the AC9 C terminus wraps around the kinase and inserts into the active site, inhibiting it. ERK7 orthologs are found in all eukaryotes with ciliated cells, though the pathways it regulates are largely unknown. Furthermore, ERK7 is autoactivating (18), raising the question how this ancient kinase is regulated. Here, we have identified an essential inhibitory interaction for the *T. gondii* ERK7. Moreover, our data highlight a simple competitive mechanism by which protein–protein interactions can ensure the fidelity and specificity of a signaling network.

Results

Loss of AC9 Blocks Host Cell Invasion and Egress and Parasite Conoid Assembly. AC9 (TGGT1_246950) was initially identified by proximity biotinylation as an apically localized interactor of the IMC suture component ISC4 (19), though AC9 function was not further investigated in the previous study. We were unable to obtain an AC9 knockout parasite strain using CRISPR-Cas9, and thus we chose to assess its function using the auxin-inducible degron (AID) system (20, 21). We endogenously tagged the C terminus of AC9 with an AID-3×HA (hemagglutinin) tag ($AC9^{AID}$). $AC9^{AID}$ faithfully localized to the apical cap (Fig. 1*A*) and addition of 3-indoleacetic acid (IAA) ($AC9^{AID/IAA}$) resulted in efficient degradation of the protein (Fig. 1*A* and *SI Appendix*, Fig. S1*A*). Loss of AC9 completely blocked the parasites' ability to form plaques, which was rescued by the expression of a non-degradable copy of AC9 (Fig. 1*B*). We found that $AC9^{AID/IAA}$ parasites replicated normally but failed to egress from their host cells. Instead, $AC9^{AID/IAA}$ parasites appeared to replicate until their vacuoles separated from the monolayer, which we found floating in the medium (Fig. 1*C*). This phenotype is similar to the knockout of parasite perforin-like protein 1 (22), and suggested a block in egress. Egress can be induced by treatment with the calcium ionophore A23187 (23). While $AC9^{AID}$ parasites efficiently egressed from host cells after ionophore treatment, $AC9^{AID/IAA}$ were completely unresponsive (Fig. 1*D*). Loss of AC9 also blocked parasite invasion of host cells (Fig. 1*E*). Invasion and egress require secretion from specialized organelles called micronemes (24). The microneme protein MIC2 is shed from the parasite plasma membrane after secretion, and the levels of this protein in media can be used as a surrogate for secretion (23). Loss of AC9 blocked both basal and ionophore-induced release of MIC2, though levels of GRA39, which is constitutively secreted through a different route, are unaffected (Fig. 1*F*). Taken together, our data show that AC9 is required for efficient microneme secretion, and its loss blocks the parasite lytic cycle.

As AC9 impacts invasion and microneme secretion, we reasoned the observed phenotypes may be due to changes in parasite ultrastructure upon AC9 degradation. To test this hypothesis, we used immunofluorescence to compare available apical markers in $AC9^{AID}$ and $AC9^{AID/IAA}$ parasites. Strikingly, loss of AC9 resulted in a disorganization of the rhoptry secretory organelles (Fig. 2*A*). These organelles are usually bundled and polarized with their necks pointing apically (marked by RON11). In $AC9^{AID/IAA}$ parasites, however, the rhoptries are detached from the parasite's apex and the necks are no longer consistently apically oriented (Fig. 2*A*). Thus, both the micronemes and rhoptries are impacted in the absence of AC9. In *Toxoplasma*, a tubulin-rich structure called the conoid forms the core of the apical complex (8) and is the site at which microneme and rhoptry secretion is thought to occur (9, 25). Partial disruptions in the conoid structure have recently been associated with loss of parasite motility, invasion, and egress (26–28). Thus, we tested whether the conoid marker SAS6L (4) was altered upon AC9 degradation. In normally developed $AC9^{AID}$ parasites, we observed distinct apical SAS6L foci in both mother and developing daughter parasites (Fig. 2*B*). Strikingly, in $AC9^{AID/IAA}$ parasites, the mother SAS6L signal was missing, while the daughter cells' was maintained (Fig. 2*B*). These data strongly suggest that AC9 is required for maturation of the parasite conoid, and that the invasion and egress phenotypes we observed upon AC9 degradation (Fig. 1) are driven by conoid loss.

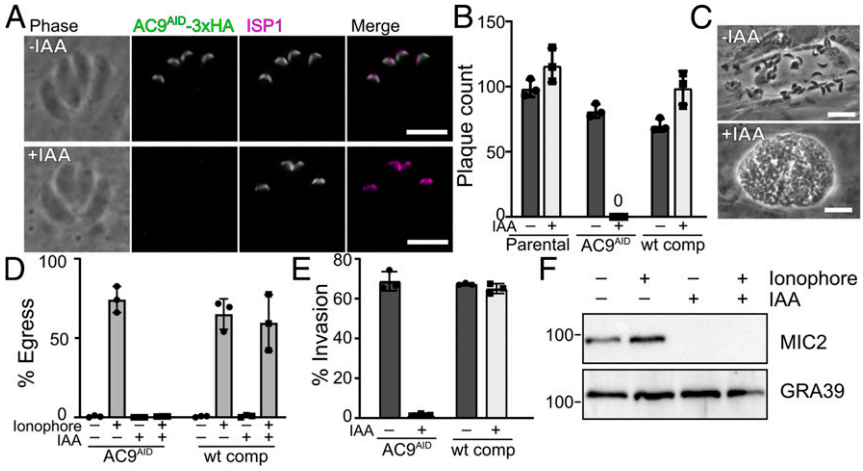

Fig. 1. AC9 is required to complete the parasite lytic cycle. (*A*) $AC9^{AID}$-3×HA (green) localizes to the apical cap (magenta) and is lost when parasites are treated with IAA. (Scale bars, 5 μm.) (*B*) Quantification of plaque number comparing growth of parental, $AC9^{AID}$, and WT-complemented $AC9^{AID}$ parasites grown with and without IAA. (*C*) $AC9^{AID}$ parasites naturally egress from host cells in −IAA but are found as floating vacuoles when grown in IAA. (Scale bars, 20 μm.) (*D*) Quantification of egress of the indicated strains induced by a calcium ionophore and grown in ±IAA. (*E*) Quantification of invasion of the indicated strains grown in ±IAA. (*F*) Western blot of soluble secreted proteins from $AC9^{AID}$ and $AC9^{AID/IAA}$. Microneme secretion was tracked with anti-MIC2 and the constitutively secreted dense granule protein GRA39 was used as a control. All error bars are SD.

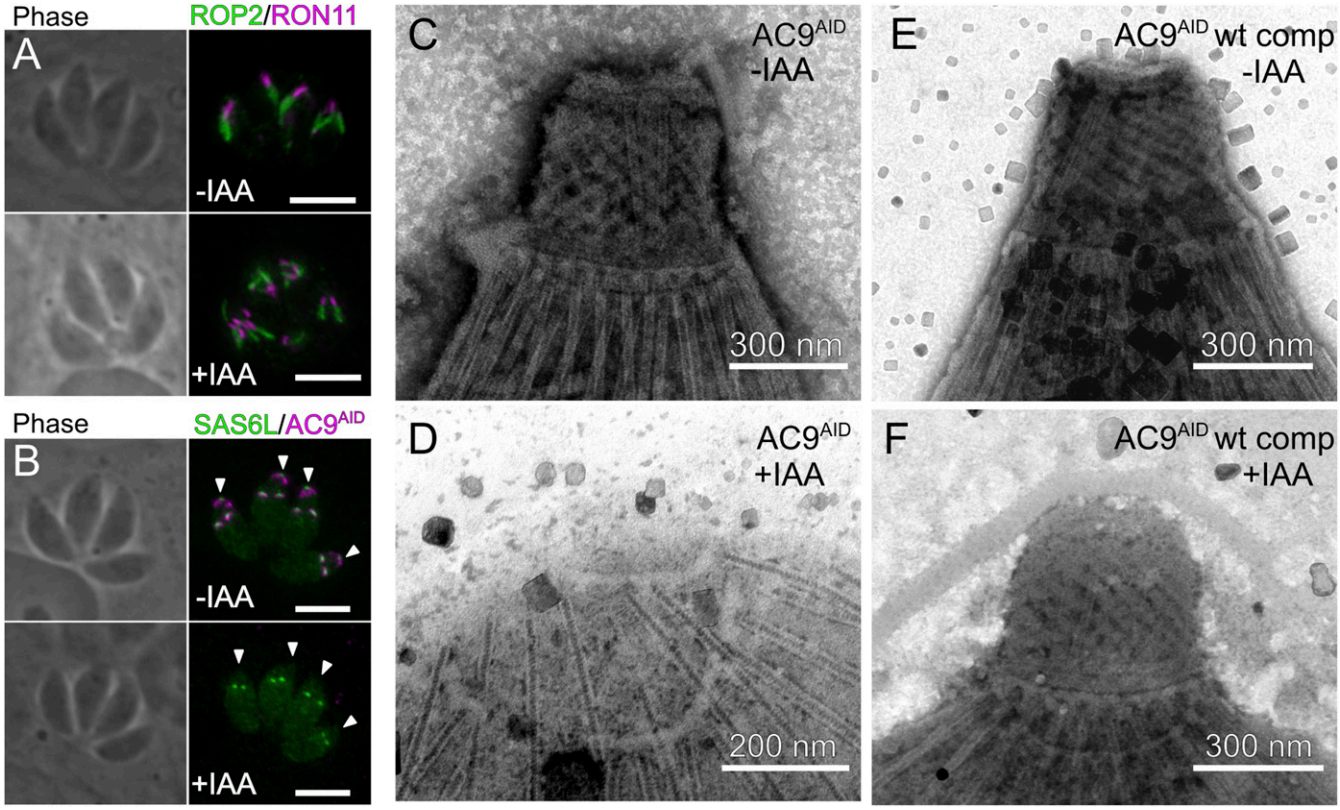

Fig. 2. Loss of AC9 disrupts the parasite apical complex. (*A*) AC9^{AID} and AC9$^{AID/IAA}$ parasites were stained with ROP2 (green) and RON11 (magenta). (*B*) AC9^{AID} and AC9$^{AID/IAA}$ parasites were stained with antibodies to the HA tag (magenta) and the conoid marker SAS6L (green). Arrowheads indicate the position of the maternal apical complex. (Scale bars, 5 μm.) (*D–F*) TEM images of the apical complex from negatively stained detergent-extracted (*C*) AC9^{AID} parasites, (*D*) AC9$^{AID/IAA}$ parasites, and AC9^{AID} WT-complemented parasites grown in (*E*) −IAA and (*F*) +IAA.

We next sought to directly examine the effect of AC9 loss on the ultrastructure of the mature parasite conoid. Many parasite cytoskeletal structures, including the apical complex, are preserved after detergent extraction (29). We detergent extracted AC9^{AID} and AC9$^{AID/IAA}$ parasites to create cytoskeleton "ghosts" and imaged them using negative-stained transmission electron microscopy (TEM). While we observed an extended conoid in AC9^{AID} parasites (Fig. 2*C*), we found that the conoid was completely absent in AC9$^{AID/IAA}$ parasites (Fig. 2*D*). As expected, expression of nondegradable AC9 rescued this phenotype (Fig. 2 *E* and *F*). Importantly, the ultrastructural changes appear to be specific to the loss of the conoid in AC9$^{AID/IAA}$ parasites, as our TEM images show that the parasites have maintained their 22 cortical microtubules (Fig. 2*D*). Intriguingly, we noted that AC9^{AID} tagging appears to have exacerbated an artifact of EM sample preparation of the parasite cytoskeleton in which the base of the conoid partially detaches from the apical polar ring (*SI Appendix*, Fig. S1). We assessed the basal (−IAA) level of AC9^{AID} protein, and found that AC9^{AID} levels are ∼40% of the levels of AC9 tagged with only a 3×HA in the same OsTIR1-expressing parental line (*SI Appendix*, Fig. S1). Such basal degradation has been uncovered as a common artifact of the AID system (30, 31). Notably, AC9^{AID}(wild-type [WT] complement) conoids were indistinguishable from the parental strain, suggesting that reduced AC9 protein levels may be driving the apparent defect in conoid ultrastructure (Fig. 1 and *SI Appendix*, Fig. S1). Nevertheless, despite any potential structural differences, the AC9^{AID} parasites showed no phenotype in secretion, invasion, or egress when untreated with IAA, in stark contrast to the effect of complete AC9 degradation (Fig. 1). Taken together, our data indicate AC9 has a critical role in maintaining apical complex ultrastructure.

Proximity Biotinylation Reveals AC9 Interacts with the MAP Kinase ERK7. We next sought to identify protein partners that collaborate with AC9 to facilitate parasite conoid assembly and/or maintenance. To this end, we endogenously tagged the protein with BirA* (AC9^{BioID}) (12, 32). After 24-h growth in 150 μM biotin, we could detect biotin labeling in the apical cap with fluorescent streptavidin, demonstrating active BirA* at this location (*SI Appendix*, Fig. S2*A*). While AC9 is predicted to be ∼70% intrinsically disordered, it has an ∼150-residue N-terminal predicted coiled-coil domain, which we reasoned may indicate it is a component of the IMC cytoskeleton. The IMC cytoskeleton is stable after detergent extraction (19), and we found that AC9 copurified with cytoskeletal, rather than membranous, components of the IMC (*SI Appendix*, Fig. S2*B*). This demonstrates AC9 is associated with the intermediate filament cytoskeleton of the apical cap, which we exploited to increase the specificity of our biotin identification (BioID) experiments (*SI Appendix*, Fig. S2*B*). We grew AC9^{BioID} parasites in biotin, lysed them in 1% Triton X-100, and separated the cytoskeleton from solubilized membrane and cytosolic components by sedimentation at 14,000 × *g*. We then purified the biotinylated proteins using streptavidin resin, which were identified by liquid chromatography-tandem mass spectrometry (LC-MS/MS) (Dataset S1). Our dataset was of high quality, as the top candidates were enriched in known apical cap proteins (12, 19). In addition, our top hit was previously undescribed (TGGT1_292950). To validate that TGGT1_292950 is, indeed, an apical cap protein, we epitope tagged the endogenous gene with 3×HA. The resulting protein colocalizes with the

apical cap marker ISP1 (*SI Appendix*, Fig. S2*C*), leading us to name the gene apical cap protein 10 (AC10).

Among the top candidates from our BioID dataset was the MAP kinase ERK7 (TGGT1_233010). We recently demonstrated that ERK7 localizes to the apical cap, and that its loss-of-function phenotype is essentially identical to what we have observed for AC9 (17). We therefore prioritized investigating the function of this interaction. AC9 and ERK7 colocalize at the apical cap (Fig. 3*A*) and proximity-ligation immunofluorescence (33) demonstrated that they are closely associated at this site (Fig. 3*B*). ERK7 is a member of an early-branching MAPK family that is conserved throughout eukaryotes (34, 35) and has been implicated as a facilitator of ciliogenesis in Metazoa (15, 16) and Apicomplexa (17), though little is known about its signaling cascade and regulatory interactions in any organism. AC9 is conserved among coccidian parasites, though the overall protein sequences are highly divergent (21 to 55% identity). The region of highest conservation is in the AC9 C terminus (Fig. 3*C*). Analysis across all sequenced coccidian genera demonstrated that 16 of the most C-terminal 33 residues in AC9 are invariant.

To test whether the AC9 C terminus was indeed the site of ERK7 binding, we bacterially expressed and purified several AC9 constructs N-terminally fused to yeast SUMO as a carrier protein. We found that $AC9_{401–452}$ was robustly pulled down by the glutathione S-transferase (GST)-ERK7 kinase domain (*SI Appendix*, Fig. S3), demonstrating that the two proteins interact directly. The AC9 C terminus is predicted to be intrinsically disordered, suggesting that it associates with the ERK7 kinase domain in an extended conformation. MAPKs interact with their substrates and regulatory partners through docking interactions that involve short linear motifs, usually 10 to 15 residues (36–38). We reasoned AC9 may be interacting through such a motif and tested whether shorter regions of the AC9 C terminus were sufficient to bind ERK7. Surprisingly, we found that neither $AC9_{401–430}$ nor $AC9_{431–452}$ were detectable after pull down by GST-ERK7 (*SI Appendix*, Fig. S3). We therefore reasoned that the entire well-conserved portion of AC9, comprising $AC9_{419–452}$ (Fig. 3*C*), was required for the interaction. We measured the binding of fluorescein-labeled $AC9_{419–452}$ to recombinantly express and purify ERK7 kinase domain by fluorescence anisotropy. $AC9_{419–452}$ bound ERK7 with a K_D of 34 ± 2 nM (Fig. 3*D*),

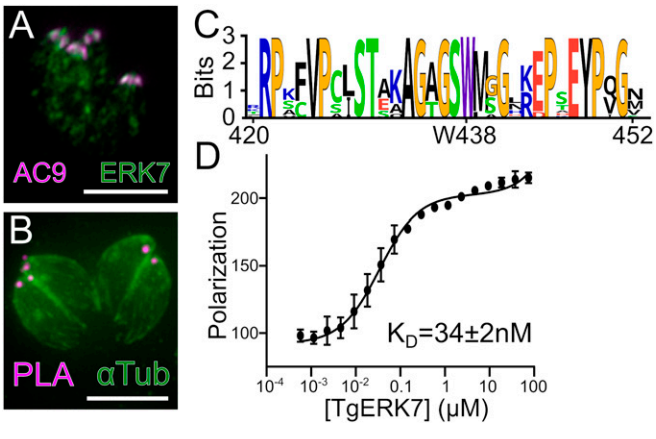

Fig. 3. AC9 tightly binds ERK7. (*A*) ERK7-Ty (green) colocalizes with AC9-HA (magenta) at the apical cap. (*B*) Proximity ligation (magenta) of ERK7 and AC9 reveal bright foci at the parasite apical cap. Parasites are counterstained with anti–β-tubulin (note that this antibody does not stain the apical complex, likely due to antigen accessibility). (Scale bars, 5 μm.) (*C*) Sequence logo for $AC9_{419–452}$ highlights invariant C-terminal residues. (*D*) Binding of $AC9_{419–452}$ to $ERK7_{1–358}$ was measured by fluorescence polarization and the K_D was calculated from global fit of three replicate experiments of three technical replicates each.

which is an affinity consistent with a strong MAPK docking-site interaction (36, 39).

AC9 Is Required for ERK7 Localization and Function in Parasites. Given their interaction, we reasoned that AC9 may be an ERK7 substrate. Available phosphoproteomic data report nine phosphosites on AC9 [ToxoDBv46, https://toxodb.org/toxo/ (40)]. To test the relevance of these sites to our observed phenotypes, we complemented the $AC9^{AID}$ strain by expressing a nonphosphorylatable allele, in which each of these Ser/Thr had been mutated to Ala (*SI Appendix*, Fig. S4*A*). This mutant protein correctly localized to the apical cap (*SI Appendix*, Fig. S4*B*) and fully rescued the ability of the $AC9^{AID}$ parasites to form plaques (*SI Appendix*, Fig. S4*C*), demonstrating that phosphorylation of these sites is not required for AC9 function.

We identified ERK7 as a component of the cytoskeletal fraction of AC9-interacting proteins (*SI Appendix*, Fig. S2 and Dataset S1), but ERK7 has no domains that would be predicted to interact with the cytoskeleton on its own. We therefore reasoned that AC9 may act as a scaffold that recruits ERK7 to the apical cap cytoskeleton. Consistent with this model, the ERK7 protein was lost from the apical cap upon AC9 degradation (Fig. 4*A*), and this localization is rescued in the AC9 WT complement (Fig. 4*B*). Importantly, AID-mediated degradation of ERK7 has no effect on AC9 localization (*SI Appendix*, Fig. S5*A*). These data suggest that a major function of AC9 is to recruit ERK7 to the apical cap. To directly test this model, we sought an AC9 mutant that retained its own localization but did not bind ERK7. While we were unable to obtain stable strains expressing deletions of the AC9 C terminus, we found that mutation of three Ser/Thr to Glu ($AC9^{3×Glu}$; Ser419-Glu, Thr420Glu, Ser437Glu) reduced in vitro AC9 affinity for ERK7 by ∼200-fold (Fig. 4*C*). $AC9^{3×Glu}$ localized correctly when expressed in the background of the $AC9^{AID}$ strain (Fig. 4 *D* and *E*), though it was unable to rescue the $AC9^{AID/IAA}$ plaque phenotype (Fig. 4*F*). In addition, while ERK7 localized to the apical cap in $AC9^{AID/3×Glu}$ parasites, this localization was lost upon addition of IAA and degradation of the wild-type $AC9^{AID}$ copy (Fig. 4*D*), as was the tubulin-rich conoid (Fig. 4*E* and *SI Appendix*, Fig. S5*B*). Therefore, interaction with AC9 is necessary for ERK7 concentration at the apical cap. Importantly, ERK7 protein was still found in the parasite cytosol after AC9 degradation, demonstrating that expression of ERK7 is not sufficient for conoid development (Fig. 4*E* and *SI Appendix*, Fig. S5*B*). These data suggest that ERK7 must be present at the apical cap to function, and demonstrate that a critical function for AC9 is to control ERK7 localization.

AC9 Binds ERK7 in an Unusual Inhibitory Conformation. To better define the nature of the AC9–ERK7 interaction, we solved the cocrystal structure of $AC9_{419–452}$ bound to the ERK7 kinase domain to 2.1 Å (Fig. 5 and *SI Appendix*, Table S1). To our surprise, the AC9 C terminus forms extensive contacts with ERK7 and wraps around the kinase from the MAPK docking site (the CD domain) to the substrate-recognition region (Fig. 5). Strikingly, AC9 binding encompasses all major MAPK-interacting and regulatory regions except for the F site (41). MAPK docking-site interactions are typically defined by a cluster of positively charged residues in the docking motif that interact with an acidic cluster in the kinase CD domain adjacent to van der Waals interactions between complementary hydrophobic surfaces in the two partners (36, 42, 43). Remarkably, the only MAPK-interacting protein from *Toxoplasma* previously described is a secreted effector, GRA24, that binds mammalian p38 with a canonical docking-site interaction (44); there are no regulatory partners known for the parasite's MAPKs.

In stark contrast to more typical docking-site interactors, AC9 does not make extensive side-chain interactions with the MAPK CD domain. AC9 Phe424, Val425, and Leu428 make weak van der Waals interactions with the ERK7 CD domain (contacts >3.5 Å).

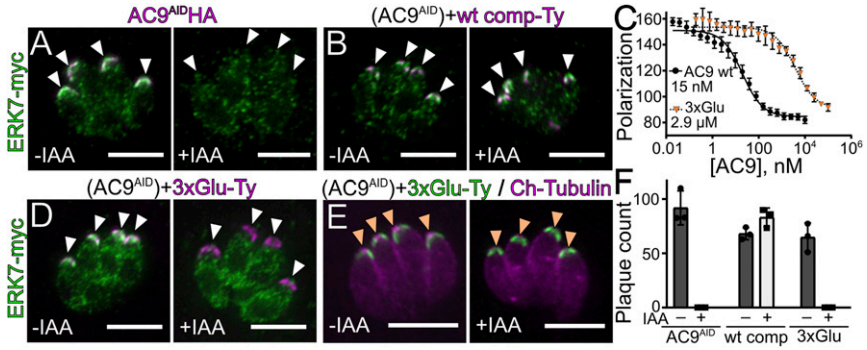

Fig. 4. AC9 is a scaffold that drives ERK7 apical localization. (*A* and *B*) ERK7-3×myc (green) localization is lost upon degradation of (*A*) $AC9^{AID}$-3×HA with growth in IAA (magenta), which is rescued in the (*B*) AC9 WT complement. White arrowheads indicate the apical cap. (*C*) K_i of WT $AC9_{401–452}$ and 3×Glu $AC9_{401–452}$ was determined by competition with fluorescein-labeled $AC9_{419–452}$; 95% CI: WT, 13.4 to 17.7 nM; 3×Glu, 2.4 to 3.6 μM. (*D*) ERK7-3×myc (green) localization was compared in 3×Glu-complemented (magenta) parasites as in *A* and *B*. (*E*) Growth of 3×Glu-complemented (green) $AC9^{AID}$ parasites expressing mCherry-tubulin (magenta) with or without IAA. Orange arrowheads indicate the expected location of conoid foci. (*F*) Quantification of plaque number comparing growth of $AC9^{AID}$, WT-complemented $AC9^{AID}$, and 3xGlu-complemented $AC9^{AID}$ parasites grown with and without IAA. (Scale bars, 5 μm.) All error bars are SD.

Only two polar AC9 side chains make close contact with the ERK7 CD domain (Fig. 5*B* and *SI Appendix*, Fig. S6): AC9 Arg421 is salt bridged with ERK7 Glu147 (3.0 Å), while AC9 Thr430 hydrogen bonds with ERK7 Glu96 (2.3 Å). Most of the ERK7 side chains in the CD domain that interact with AC9 do so through backbone hydrogen bonds. Mutation of the "basic patch" (e.g., MNK Arg5, Lys6 in Fig. 5*C*) of typical motifs that bind the MAPK CD domain abrogates their binding (36). Consistent with the idea that AC9 forms a suboptimal ERK7 docking-site interaction, mutation of the two basic residues in the AC9 CD-interacting motif (Arg421 and Lys423) to Ala only reduces affinity for ERK7 by approximately fourfold (Fig. 5*H*).

The C-terminal nine residues of AC9 (444 to 452) appear to act as a pseudosubstrate, as these residues make close contacts with the ERK7 substrate-recognition subdomain (Fig. 5*D*). These interactions are centered around the invariant AC9 Pro449, which appears to mimic the required Pro in a true MAPK substrate and packs against ERK7 Trp185 (3.4 Å). Intriguingly, the C terminus of AC9 makes contacts with a conserved basic cluster (ERK7 Arg184, 2.8 Å; Arg187, 2.9 Å) adjacent to the kinase APE motif. This cluster normally coordinates the pTyr in active MAPKs (Fig. 5*E*), indicating AC9 binding partially displaces the ERK7 activation loop. Notably, the ERK7-binding motif in AC9 is of an invariant length at the C terminus in all AC9 sequences (Fig. 3*C*) and the interaction with the AC9 C-terminal carboxylate helps explain this conservation.

Most striking of the AC9 interactions with ERK7, however, is the insertion of AC9 Trp438 into the ERK7 active site (Fig. 5*F*). The Trp438 side chain has displaced nucleotide and Mg^{2+} in our structure; even though the crystals formed in 1 mM ADP and 10 mM $MgCl_2$, there is no density consistent with either. In fact, the Trp438 side chain appears to be acting as a nucleotide mimic, a surprising function for a protein residue. The Trp438 indole ring makes π–cation interactions (3.2 Å) with the catalytic VAIK Lys42 that normally coordinates the ATP β-phosphate. In addition, the indole ring hydrogen bonds with the DFG Asp154 (2.7 Å), which normally coordinates nucleotide through a bound Mg^{2+}. The AC9 loop flanking Trp438 inserts from above the ERK7 CD domain, pushing the kinase Gly loop into an open conformation without disrupting its overall secondary structure. Thus, the AC9-bound conformation of the ERK7 active site is substantially different from that typical of an active kinase, such as ERK2 (Fig. 5*G* and *SI Appendix*, Fig. S7 *A* and *B*). Furthermore, our structure fully explains the loss of affinity of the $AC9^{3×Glu}$ mutant for ERK7. While neither Ser419 nor Thr420 makes side-chain contacts, Ser437 is buried in the active site next to Trp438. Mutation of Ser437 to Glu, however, would clash with ERK7 Asp98 (*SI Appendix*, Fig. S7*C*), consistent with the 200-fold drop in affinity we observed.

Taken together, our structural data strongly suggested that AC9 acts not only as a scaffold for ERK7 but likely serves as a competitive inhibitor of its kinase activity. Indeed, we found that *Toxoplasma* ERK7 phosphorylation of the generic substrate myelin basic protein (MBP) was completely blocked by the addition of 10 μM $AC9_{401–452}$ to the reaction (Fig. 6*A*). Because the interactions AC9 makes with *Toxoplasma* ERK7 side chains are broadly conserved among MAPKs (*SI Appendix*, Fig. S6), we reasoned AC9 may be a promiscuous inhibitor. Surprisingly, this was not the case. While AC9 robustly inhibits *Toxoplasma* ERK7 activity, it had no effect on the ability of another *Toxoplasma* MAPK (TgMAPK2), rat ERK7, or rat ERK2 to phosphorylate MBP (Fig. 6*A*). It thus seems likely that the specificity of AC9 for TgERK7 is due to a combination of surface complementarity and the ability of TgERK7 to adopt a conformation able to recognize AC9.

As described above, AC9 binds ERK7 with an extended interface that buries ∼1,650 $Å^2$. While the AC9–ERK7 interaction is reasonably strong (15 to 35 nM; Figs. 3*D* and 4*C*), protein–peptide interactions can achieve similar affinities with substantially smaller buried surfaces. For instance, Grb2-SH2 binds $Shc1_{423–435}$ with a K_D of 18 nM (45) with a 404-$Å^2$ interface (46). Similarly, the Cbl-TKB domain binds $APS_{609–621}$ with a K_D of 43 nM with a 629-$Å^2$ interface (47). These data suggest the AC9–ERK7 interface is formed by a distributed series of weak interactions, which is consistent with our mutagenesis data. Mutation of residues usually critical to recognizing the MAPK CD domain only modestly affected AC9 affinity ($AC9_{R231A/K232A}$; Fig. 5*H*). Even mutation of Trp438 yielded a protein with a respectable, albeit weakened, affinity of 1.6 μM (Fig. 5*H*). In addition, these distributed interactions (CD domain, active site, activation loop/pseudosubstrate) appear to act cooperatively to enable AC9 to capture ERK7 in an optimal conformation for binding. Truncated versions of AC9 showed no measurable binding to the kinase (*SI Appendix*, Fig. S3).

Given these observations, we reasoned that AC9 may be displaced by a substrate that can engage the CD domain with a physiologically relevant affinity. While there are yet no known substrates of *Toxoplasma* ERK7, we tested available peptides with known affinities to metazoan MAPKs for ERK7 binding. Even though there is no homologous sequence in *Toxoplasma*, we found that rat $MEK2_{4–16}$ binds *Toxoplasma* ERK7 with a K_D of ∼12 μM (Fig. 6*B*). Note that physiological MAPK docking-site interactions range in affinity from 0.5 to 50 μM (39, 48, 49) and MEK2 engages its cognate partner, ERK2, with an ∼8 μM K_D.

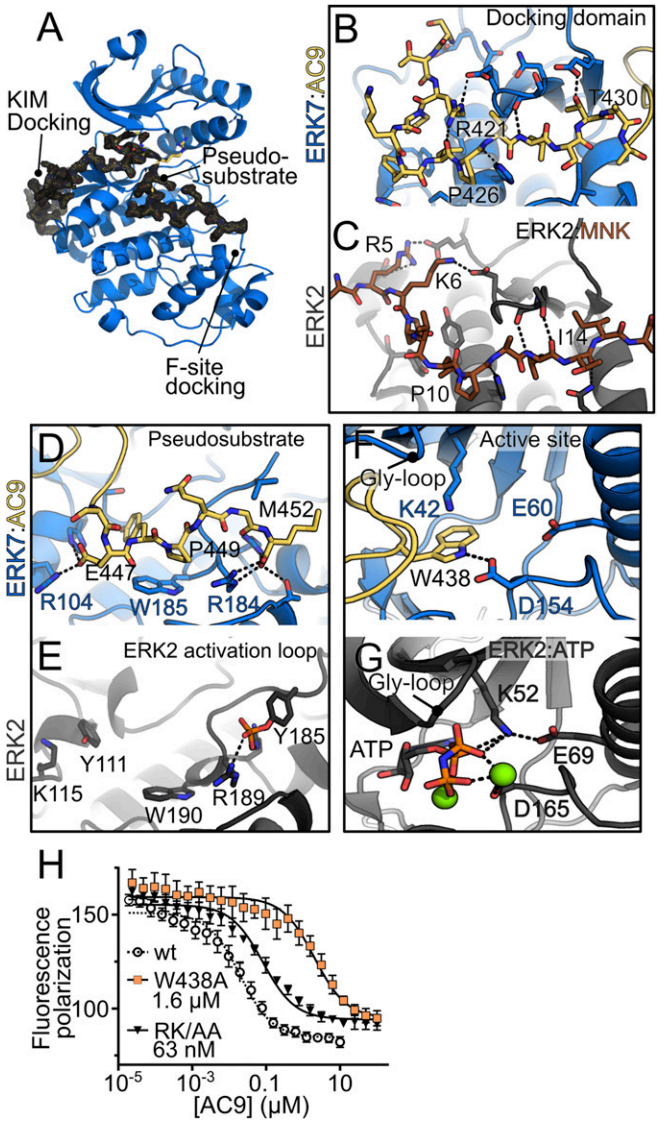

Fig. 5. AC9 binds ERK7 in an inhibitory conformation. (*A*) Overview of AC9–ERK7 interaction. ERK7 is blue. A 1.5σ $2F_O - F_C$ electron density map (black) is shown around AC9 (yellow). (*B–G*) Contacts between AC9 (yellow) and ERK7 (blue) are compared with ERK2 (gray) at (*B* and *C*) the MAPK-docking domain, (*D* and *E*) activation loop/substrate binding site, and (*F* and *G*) kinase active site. (*H*) K_I of AC9 mutants was determined by competition with fluorescein-labeled wild-type AC9. Wild-type competition curve (K_I 15 nM) is shown for comparison; 95% CI: $AC9_{W438A}$, 1.3 to 2.0 μM; $AC9_{R421A/K423A}$ (RK/AA), 55 to 74 nM. ERK2 images are from PDB ID codes 4H3Q (*C*) and 6OPG (*E* and *G*). All error bars are SD.

We chose to modify a well-characterized mammalian MAPK substrate, ELK1, which requires CD-domain interaction for efficient phosphorylation (50). As expected, we could not detect measurable phosphorylation of an $ELK1_{300–428}$ construct, which lacks an ERK7-binding motif. A chimeric ELK1 construct that contains the MEK2-docking motif ($ELK1_{MEK2\text{-}D}$), however, was phosphorylated by ERK7 at levels similar to the generic substrate MBP in the absence of AC9 (Fig. 6*C*). While ERK7 phosphorylation of MBP was efficiently inhibited by AC9, substantial levels of $ELK1_{MEK2\text{-}D}$ phosphorylation remained even in the presence of 10 μM AC9 (Fig. 6*C*). Thus, AC9 inhibition of ERK7 can be successfully released by competition with even a modest-affinity docking-site interaction.

Notably, ERK7 family members are unusual in the MAPK family as they are able to autophosphorylate their activation loops (18), and thus bypass the need for a MAPK kinase for their activation. We have previously found that ERK7 kinase activity is required for conoid formation (17). Our data therefore suggest that AC9 has the dual roles of concentrating *Toxoplasma* ERK7 at the apical cap and regulating its kinase activity and substrate specificity (Fig. 6*D*).

Discussion

We have identified AC9 as an essential cytoskeletal scaffold of the *Toxoplasma* ERK7 kinase. Remarkably, inducing AC9 degradation phenocopies loss of ERK7 and results in parasites that mature without conoids, thereby interrupting the lytic cycle. We found that AC9 is required for ERK7 localization to the apical cap and identified a mutant that could not bind and recruit ERK7, and therefore did not rescue any of the AC9 loss-of-function phenotypes (Fig. 4). Surprisingly, our crystal structure of the ERK7–AC9 complex revealed that AC9 is also a competitive inhibitor of ERK7 kinase activity. Usually, genetic ablation of an inhibitor would be expected to present the opposite phenotype from its target. Because ERK7 kinase activity is required for conoid formation (17), our data suggest that AC9 inhibition of the kinase is not permanent. Instead, we propose that AC9 binding to ERK7 represents an unusual mechanism of ensuring kinase specificity (Fig. 6*D*). Because ERK7 is autoactivating, its regulation by a phosphatase would be insufficient to ensure signaling fidelity, especially when the kinase is maintained at a high local concentration at the apical cap. While the full AC9 C terminus binds tightly to ERK7 (Fig. 3*D*), this is due to cooperative binding of distributed contacts (Fig. 5); neither $AC9_{401–430}$, which occupies the CD domain, nor $AC9_{431–452}$, which occupies the active and pseudosubstrate sites, is sufficient for ERK7 binding (*SI Appendix*, Fig. S3). We therefore propose that an ERK7 substrate with both a strong kinase-interacting motif and substrate site would successfully compete with AC9 for kinase binding during phosphorylation (Fig. 6*D*). Alternatively, an ERK7-activating factor may transiently displace AC9, allowing substrate binding. In either of these cases, the regulated release of AC9 inhibition would define ERK7 activity. Determining ERK7 substrates as well as other regulatory factors will not only provide the opportunity to directly test these models but will also allow us to define how ERK7 facilitates ciliogenesis in parasites (17) and other organisms (15, 16).

A striking feature of the AC9 inhibition of ERK7 is its specificity. Even though AC9 makes contacts with conserved sites, we found that it does not inhibit other *Toxoplasma* or mammalian MAPKs, including the rat ERK7 ortholog. These data suggest that the kinase dynamics, rather than final contact sites, are contributing to specificity of the inhibition. This has clear implications for the design of specific inhibitors of parasite ERK7. Moreover, the AC9–ERK7 interaction may represent a generalized mechanism of inhibiting ancient signaling molecules such as ERK7. ERK7 is the earliest-branching member of the MAPK family (51), and is unusual in its autoactivation (18). Notably, cyclin-dependent kinases (CDKs) are also regulated by inhibitory proteins (52), and are related to the MAPKs (51). Like the ERK7–AC9 interaction, the cell-cycle inhibitor p27 is intrinsically disordered and binds CDK2 through a distributed surface. Also like AC9, p27 inserts itself into the kinase active site and displaces nucleotide (*SI Appendix*, Fig. S7*C*) (53). However, there are notable differences between the two inhibitory interactions. First, AC9 occupies the MAPK CD domain, which is not present in CDKs. Also, while our structure demonstrates that AC9 insertion pushes the ERK7 Gly loop into an inactive conformation (Fig. 5 and *SI Appendix*, Fig. S7), p27 replaces the first β-strand in CDK2, destroying the Gly-loop structure (*SI Appendix*, Fig. S7*C*). Finally, while both ERK7 and AC9 protein levels appear to be maintained stably at the apical cap throughout the cell cycle, p27 is degraded

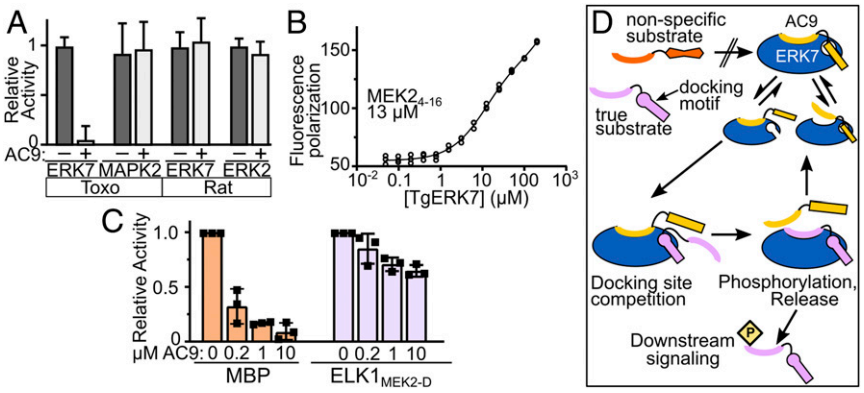

Fig. 6. AC9 is an inhibitory regulator of ERK7 kinase activity. (*A*) Quantification of phosphorylation of MBP by the indicated kinases in the presence and absence of 10 μM $AC9_{401–452}$, normalized to activity without AC9. (*B*) Binding of kinase-interacting-motif from rat MEK2 to TgERK7 was measured by fluorescence polarization; 95% CI: 10.5 to 14.5 μM. (*C*) Quantification of TgERK7 phosphorylation of MBP or a chimeric ELK1/$MEK2_{4–16}$ substrate in the presence of the indicated $AC9_{401–452}$ concentration ($n = 3$ biological replicates). (*D*) Model for AC9 regulation of ERK7 specificity. AC9 occupies the ERK7 active site, preventing the binding of nonspecific substrates. However, the AC9 docking-site interaction is suboptimal and can be competed off by true ERK7 substrates, which are released after phosphorylation, allowing AC9 to rebind. All error bars are SD.

at the G_1/S transition, releasing its inhibition of CDK2 (54). Nevertheless, the convergent evolution of specific protein inhibitors of two branches of the CMGC family suggests that there may be additional genetically encoded kinase inhibitors that remain unidentified throughout Eukaryota. Identifying such inhibitors would refine our understanding of cellular signaling architecture and provide potential platforms on which specific therapeutics may be designed.

Materials and Methods

Sequence Analysis. Sequences for AC9 from *T. gondii*, *Hammondia hammondi*, *Neospora caninum*, *Cyclospora cayetanensis*, *Cystoisospora suis*, *Eimeria* spp., and *Sarcocystis neurona* were retrieved from ToxoDBv43 (https://toxodb.org/toxo/) using the basic local alignment search tool (BLAST). The AC9 sequence from *Besnoitia besnoiti* was identified by BLAST and retrieved from UniProt. The protein sequences were aligned with Clustal Omega (55). The AC9 sequence logo was generated with WebLogo (56).

PCR and Plasmid Generation. All PCRs were conducted using Phusion polymerase (NEB) using primers listed in Dataset S2. Constructs were assembled using Gibson master mix (NEB). Point mutations were created by the Phusion mutagenesis protocol. $AC9^{AID}$ tagging constructs were generated using a PCR-amplified homology-directed repair template (P1-2) and a CRISPR-Cas9 pU6-Universal plasmid with a protospacer against the 3′ untranslated region of the gene of the interest (P3-4). AC9-BirA*, ERK7, and AC10 C-terminal tagging constructs were generated using P1-4, P5-8, and P9-12, respectively. To generate the wild-type complementation construct, the complete AC9-coding sequence was PCR-amplified from complementary DNA and cloned into a UPRT-locus knockout vector driven by the ISC6 promoter. Both the 3×Glu and the phosphorylation mutants were constructed using synthetic genes (Quintara Biosciences) and cloned into the pISC6-UPRT vector (Dataset S2).

Chemicals and Antibodies. 3-Indoleacetic acid (heteroauxin; Sigma-Aldrich; I2886) was used at 500 μM from a 500 mM stock in 100% ethanol. A23187 (Sigma-Aldrich; C5722) was used at 1 to 2 μM, dissolved from a 2 mM stock in dimethyl sulfoxide (DMSO). The HA epitope was detected with mouse monoclonal antibody (mAb) HA.11 (BioLegend; MMS-101P), rabbit polyclonal antibody (pAb) anti-HA (Invitrogen; 71-5500), or rat monoclonal 3F10 (Sigma-Aldrich; 11867423001). The Ty1 epitope was detected with mouse mAb BB2 (57). The c-Myc epitope was detected with mouse mAb 9E10 (58) or rabbit pAb anti-Myc (Invitrogen; PA1981). His_6-tagged proteins were recognized with mouse anti-His_6 (R&D Systems; MAB050). Biotinylated proteins were detected with Alexa Fluor 488-streptavidin (Molecular Probes; S32354) and captured with Streptavidin High-Capacity Agarose Beads (Thermo Scientific; PI20359). *Toxoplasma*-specific antibodies include rabbit anti–β-tubulin (17), mouse mAb anti-ISP1 7E8 (11), rabbit pAb anti-SAG1 (59), mouse mAb anti–F1-ATPase beta subunit 5F4 (60), mouse mAb anti-MIC2 (gift from Vern Carruthers, University of Michigan, Ann Arbor, MI), rat pAb anti-GRA39 (61), rabbit pAb anti-ROP2, rat pAb anti-RON11 (60), mouse mAb anti-SAS6L (4), mouse mAb anti-IMC1 45.15 (62), and mouse mAb anti-ISP3 (11).

Immunofluorescence. Human foreskin fibroblasts (HFF) were grown on coverslips in 24-well plates until confluent and were infected with parasites. The cells were rinsed once with phosphate-buffered saline (PBS), fixed with 3.7% formaldehyde in PBS, washed, permeabilized with 0.1% Triton X-100, blocked with 3% bovine serum albumin (BSA) for 1 h, and incubated with primary antibodies for a minimum of 2 h. Secondary antibodies used were conjugated to Alexa Fluor 488 or Alexa Fluor 594 (Thermo Scientific). The coverslips were mounted in Vectashield (Vector Labs) and viewed with an Axio Imager.Z1 fluorescence microscope (Zeiss). For proximity-ligation assays, cells were fixed in 4% paraformaldehyde/4% sucrose followed by permeabilization in 0.1% Triton X-100 for 10 min. Blocking, antibody incubations, and proximity ligation were conducted according to the manufacturer's directions (Sigma-Aldrich) using rabbit polyclonal anti-HA (63) and mouse m2 anti-FLAG (Sigma-Aldrich; F1804) as primary antibodies. Cells were counterstained with Alexa Fluor 647-conjugated rabbit anti–β-tubulin, mounted in Vectashield, and imaged on a Nikon Ti2E microscope.

Western Blotting. Parasites were lysed in Laemmli sample buffer with 100 mM dithiothreitol (DTT) and heated at 100 °C for 10 min. Proteins were separated by sodium dodecyl sulfate/polyacrylamide-gel electrophoresis (SDS/PAGE), transferred to nitrocellulose, and probed with primary antibodies and the corresponding secondary antibody conjugated to horseradish peroxidase. Western blots were imaged using SuperSignal West Pico Substrate (Pierce) and imaged on a ChemiDoc XRS+ (Bio-Rad). Band intensities were quantified using the manual volume tool in the Image Lab Software of ChemiDoc XRS+.

Plaque Assays. HFF monolayers were supplemented with ±500 μM IAA before allowing equal numbers of freshly lysed, extracellular parasites of a given strain (grown in −IAA) to infect and form plaques for 7 d. Cells were then fixed with ice-cold methanol and stained with crystal violet. Plaque number was counted manually and analyzed by Prism (GraphPad). All plaque assays were performed in triplicate for each condition.

Invasion Assays. Invasion assays were performed as previously described (22). Parasites were grown for 30 h ±IAA and intracellular parasites were collected by scraping and passaging through a 27-gauge needle. Equivalent parasite numbers were resuspended in Endo buffer (64) and settled onto coverslips with HFF monolayers for 20 min. Endo buffer was then replaced with warm D1 media (Dulbecco's modified Eagle's medium, 20 mM Hepes, 1% fetal bovine serum) and incubated at 37 °C for 30 min. Coverslips were then fixed and blocked, and extracellular parasites were stained with anti-SAG1 antibodies. The samples were then permeabilized, and all parasites were stained with anti-F1B ATPase antibodies and incubated with secondary antibodies. Parasites were scored as invaded (SAG1+, F1B− ATPase−) or not (SAG1+, F1B+) by fluorescence microscopy. Invasion assays were performed

in triplicate, at least 10 fields were counted for each replicate, and the average for each replicate was calculated as a percentage.

Egress Assays. Parasites were grown on a monolayer on coverslips for 34 h ±IAA until most vacuoles contained 16 or 32 parasites. Coverslips were washed twice with prewarmed PBS and incubated with A23187 (or DMSO control) diluted in PBS at 37 °C for 2 min. Coverslips were then fixed and stained with rabbit anti-IMC12 antibodies. At least 10 fields of ∼200 vacuoles per field were counted for three replicate coverslips for each condition.

Microneme Secretion. Microneme-secretion assays were performed as previously described (23). Briefly, parasites were grown for 30 h and intracellular parasites were collected by mechanical release through a 27-gauge needle. After washing twice in D1 media, parasites were resuspended in prewarmed D1 media and induced with 1 μM A23187 for 10 min at 37 °C. Secretion was arrested by cooling on ice, and parasites were pelleted at 1,000 × *g* for 5 min at 4 °C. The supernatant was collected and centrifuged again at 1,000 × *g*. Secreted proteins in the resulting supernatant were assessed by SDS/PAGE and Western blot analysis.

Detergent Fractionation and Streptavidin Purification. The IMC cytoskeletal fraction was isolated by 1% Triton X-100 fractionation as described (65). Extracellular parasites were lysed in 1% Triton X-100, 50 mM Tris·HCl (pH 7.4), 150 mM NaCl buffer supplemented with cOmplete Protease Inhibitor Mixture (Roche) and incubated on ice for 30 min. Lysates were centrifuged, and equivalent loads of the total, supernatant, and pellet samples were run on SDS/PAGE and immunoblotted, using IMC1 and ISP3 as cytoskeletal and soluble controls, respectively. For streptavidin purification of BioID samples, parasites were grown for 24 h in media supplemented with 150 μM biotin. The cytoskeletal fraction was solubilized in 1% SDS and diluted to RIPA conditions, biotinylated proteins were purified using Streptavidin High-Capacity Agarose (Pierce), and the proteins were identified via mass spectrometry.

Mass Spectrometry. Purified proteins bound to streptavidin beads were reduced, alkylated, and digested by sequential addition of lys-C and trypsin proteases (66, 67). Samples were then desalted using C18 tips (Pierce) and fractionated online using a 75-μm inner-diameter fritted fused silica capillary column with a 5-μm pulled electrospray tip and packed in-house with 15 cm of Luna C18(2) 3-μm reversed-phase particles. The gradient was delivered by an EASY-nLC 1000 Ultra-High-Pressure Liquid-Chromatography System (Thermo Scientific). MS/MS spectra were collected on a Q-Exactive mass spectrometer (Thermo Scientific) (68, 69). Data analysis was performed using ProLuCID and DTASelect2 implemented in Integrated Proteomics Pipeline IP2 (Integrated Proteomics Applications) (70–72). Database searching was performed using a FASTA protein database containing *T. gondii* GT1-translated open reading frames downloaded from ToxoDB on February 23, 2016. Protein and peptide identifications were filtered using DTASelect and required a minimum of two unique peptides per protein and a peptide-level false positive rate of less than 5% as estimated by a decoy database strategy. Candidates were ranked by normalized spectral abundance factor values comparing $AC9^{BioID}$ versus control samples (73).

Transmission Electron Microscopy. To prepare parasite ghosts for TEM, parasites were first incubated with 20 μM calcium ionophore in Hank's buffered saline solution at 37 °C for 10 min. The parasite suspension was allowed to adhere to a grid, after which membranes were extracted by addition of 0.5% Triton X-100 for 3 to 4 min. The samples were then stained with 2% phosphotungstic acid (pH 7.4). All TEM images were acquired on a Tecnai G2 Spirit transmission electron microscope (FEI) equipped with an LaB_6 source at 120 kV.

Protein Expression and Purification. Unless otherwise noted, proteins were expressed as N-terminal fusions to His_6-SUMO. All proteins were expressed in Rosetta2 (DE3) bacteria overnight at 16 °C after induction with 300 mM isopropyl β-D-1-thiogalactopyranoside. TgERK7 for crystallography and binding was coexpressed with λ-phosphatase. For His_6-tagged proteins, cells were resuspended in 50 mM Tris (pH 8.6), 500 mM NaCl, 15 mM imidazole and lysed by sonication. His_6-tagged protein was affinity-purified using Ni-NTA resin (Qiagen), which was washed with binding buffer. Protein was eluted in 20 mM Tris (pH 8.6), 100 mM NaCl, 150 mM imidazole. $ERK7_{2–358}$ and AC9 constructs were further purified as follows. Protein was diluted 1:1 with 20 mM Tris (pH 8.6) and purified by anion exchange on a HiTrap Q column. The resulting peaks were pooled and incubated with ULP1 protease for 30 min, after which they were diluted 1:1 in water and the cleaved SUMO was separated from the protein of interest by anion exchange. The flow-through was concentrated and purified by size-exclusion chromatography and flash-frozen in 10 mM Hepes (pH 7.0), 300 mM NaCl for storage. GST and GST-ERK7 kinase domain (residues 2 to 358) were affinity-purified using glutathione Sepharose (GE) and eluted with 10 mM glutathione, which was removed by dialysis in storage buffer before concentration and flash freezing.

GST Pull Downs. Purified GST and GST-$ERK7_{2–358}$ were bound to glutathione Sepharose (GE) in 10 mM Hepes (pH 7.0), 300 mM NaCl, 10 mM DTT. Equimolar amounts of purified SUMO fusions of $AC9_{401–452}$, $AC9_{401–430}$, or $AC9_{431–452}$ (with an additional disordered linker composed of $AC9_{401–405}$) were incubated with the glutathione resin for 5 to 10 min and washed four times in binding buffer. The bound protein was removed by boiling in 1× SDS sample buffer, separated by SDS/PAGE, and detected by Western blot analysis with mouse anti-His_6 (Sigma).

Fluorescence Polarization. $AC9_{419–452}$ with an additional N-terminal Cys was purified as above, and allowed to react overnight with fluorescein-5-maleimide (Molecular Probes). Free fluorescein was removed by sequential buffer exchange with an ND-10 desalting column and then by a 3-kDa molecular mass cutoff centrifugal concentrator. Binding affinity was measured by serially diluting $ERK7_{2–358}$ against 10 nM fluorescein-AC9 in 20-μL volumes in a 384-well plate, and fluorescence polarization was measured in a BioTek Synergy plate reader. MEK2 binding was conducted in the same manner by titrating ERK7 against 100 nM fluorescein-labeled synthetic $MEK2_{4–16}$ peptide (gift from Melanie Cobb, University of Texas (UT) Southwestern, Dallas, TX). Competition experiments were conducted by titrating unlabeled AC9 constructs against 10 nM fluorescein-AC9 and 100 nM ERK7. All curves were globally fit in GraphPad Prism (to single-site binding or single-site inhibition, as appropriate) from biological triplicates of independent experiments composed of triplicate samples; 95% CIs for all fit affinities are indicated in the figure legends.

Protein Crystallization. A 1:1 $ERK7_{2–358}$:$AC9_{419–452}$ complex at 9 mg/mL total protein with 10 mM $MgCl_2$, 1 mM ADP, 10 mM DTT was mixed 1:1 in a sitting drop with 0.15 M DL-malic acid (pH 7.0), 20% polyethylene glycol 3350. Crystals were flash-frozen in a cryoprotectant of reservoir with 25% ethylene glycol.

Data Collection, Structure Determination, and Refinement. The diffraction data were collected at the UT Southwestern Structural Biology core with the Rigaku MicroMax-003 high-brilliancy CuK-α X-ray generator, equipped with a Rigaku HyPix direct photon detector, and processed using the CrysAlisPro software package. A model of *Toxoplasma* ERK7 was created in Modeler v9.14 (74) using Protein Data Bank (PDB) ID code 3OZ6 and used as a search model for molecular replacement in Phaser (75). Cycles of manual rebuilding in Coot (76) and refinement in PHENIX (77) led to a final 2.1-Å structure of the ERK7–AC9 complex (PDB ID code 6V6A). The structure was evaluated with MolProbity (78).

In Vitro Kinase Assays. The kinase assays comparing the specificity of AC9 inhibition were run using 1 μM indicated kinases, 5 mM $MgCl_2$, 200 μM cold ATP, 10 mM DTT, 1 mg/mL BSA, 300 mM NaCl, 20 mM Hepes (pH 7.0), 10% glycerol. TgERK7, rat ERK7, and TgMAPK2 were bacterially expressed as His_6-SUMO fusions and purified without phosphatase treatment. The coding sequence for rat ERK7 was a gift of Marsha Rosner, University of Chicago, Chicago, IL. Activated rat ERK2 was a gift of Melanie Cobb. Reactions were started by adding a hot ATP mix that contained 10 μCi [γ-^{32}P]ATP and 5 μg MBP. The 25-μL reactions were incubated at a 30 °C water bath for 30 min. Reactions were stopped by adding 9 μL 4× SDS buffer; 20-μL samples were then run on an SDS/polyacrylamide gel. The gels were Coomassie-stained, and the MBP band was excised and radioactivity was quantified using a scintillation counter. Recombinant ELK1 and $ELK1_{MEK2\text{-}D}$ were expressed as His_6-SUMO fusions and purified according to the same protocol as AC9. Competition assays were performed as above, with 200 nM TgERK7, 100 μM cold ATP, 10 μM either MBP or $ELK1_{MEK2}$ substrates, and varying concentrations of $AC9_{401–452}$. These assays were imaged by phosphorimager (FujiFilm; FLA-5100) and quantified using the ImageJ gel quantification tool (79).

Figure Generation. Data plotting and statistical analyses were conducted in GraphPad Prism v8.3. All error bars are mean-centered SD. All figures were created in Inkscape v0.92.

Data Availability. All data used in the study are included in the paper and Datasets S1 and S2 and the crystal structure of the ERK7–AC9 complex has been deposited in the PDB (ID code 6V6A). All plasmids and parasite strains developed in this study will be made available upon request.

ACKNOWLEDGMENTS. We thank Betsy Goldsmith and Melanie Cobb for guiding discussions; Vasant Muralidharan, Vinnie Taggliabracci, and Ben Weaver for helpful comments on the manuscript; the UT Southwestern Electron Microscopy core facility for assistance with data collection; and Zhe Chen and the UT Southwestern Structural Biology Lab for assistance with data collection and processing. X-ray data were collected on shared equipment funded by NIH Grant S10 OD025018. M.L.R. acknowledges funding from the Welch Foundation (I-1936-20170325) and National Science Foundation (MCB1553334). X.H. was funded, in part, by Cancer Prevention and Research Institute of Texas Training Grant RP160157. P.J.B. acknowledges funding from the NIH (National Institute of Allergy and Infectious Diseases R01 AI123360) and J.A.W. acknowledges NIH R01 GM089778. P.S.B. was funded by Ruth L. Kirschstein National Research Service Award GM007185.

1. J. F. Reiter, M. R. Leroux, Genes and molecular pathways underpinning ciliopathies. *Nat. Rev. Mol. Cell Biol.* **18**, 533–547 (2017).
2. H. Ishikawa, W. F. Marshall, Intraflagellar transport and ciliary dynamics. *Cold Spring Harb. Perspect. Biol.* **9**, a021998 (2017).
3. S. Werner, A. Pimenta-Marques, M. Bettencourt-Dias, Maintaining centrosomes and cilia. *J. Cell Sci.* **130**, 3789–3800 (2017).
4. J. C. de Leon *et al*., A SAS-6-like protein suggests that the *Toxoplasma* conoid complex evolved from flagellar components. *Eukaryot. Cell* **12**, 1009–1019 (2013).
5. R. J. Wall *et al*., SAS6-like protein in *Plasmodium* indicates that conoid-associated apical complex proteins persist in invasive stages within the mosquito vector. *Sci. Rep.* **6**, 28604 (2016).
6. M. E. Francia, J.-F. Dubremetz, N. S. Morrissette, Basal body structure and composition in the apicomplexans *Toxoplasma* and *Plasmodium*. *Cilia* **5**, 3 (2016).
7. M. E. Francia *et al*., Cell division in apicomplexan parasites is organized by a homolog of the striated rootlet fiber of algal flagella. *PLoS Biol.* **10**, e1001444 (2012).
8. K. Hu, D. S. Roos, J. M. Murray, A novel polymer of tubulin forms the conoid of *Toxoplasma gondii*. *J. Cell Biol.* **156**, 1039–1050 (2002).
9. M. G. Del Carmen, M. Mondragón, S. González, R. Mondragón, Induction and regulation of conoid extrusion in *Toxoplasma gondii*. *Cell. Microbiol.* **11**, 967–982 (2009).
10. A. Keeley, D. Soldati, The glideosome: A molecular machine powering motility and host-cell invasion by Apicomplexa. *Trends Cell Biol.* **14**, 528–532 (2004).
11. J. R. Beck *et al*., A novel family of *Toxoplasma* IMC proteins displays a hierarchical organization and functions in coordinating parasite division. *PLoS Pathog.* **6**, e1001094 (2010).
12. A. L. Chen *et al*., Novel components of the *Toxoplasma* inner membrane complex revealed by BioID. *MBio* **6**, e02357-14 (2015).
13. A. Hunt *et al*., Differential requirements for cyclase-associated protein (CAP) in actin-dependent processes of *Toxoplasma gondii*. *eLife* **8**, e50598 (2019).
14. K. Frénal *et al*., Functional dissection of the apicomplexan glideosome molecular architecture. *Cell Host Microbe* **8**, 343–357 (2010).
15. K. Miyatake, M. Kusakabe, C. Takahashi, E. Nishida, ERK7 regulates ciliogenesis by phosphorylating the actin regulator CapZIP in cooperation with Dishevelled. *Nat. Commun.* **6**, 6666 (2015).
16. A. Kazatskaya *et al*., Primary cilium formation and ciliary protein trafficking is regulated by the atypical MAP kinase MAPK15 in *Caenorhabditis elegans* and human cells. *Genetics* **207**, 1423–1440 (2017).
17. W. J. O'Shaughnessy, X. Hu, T. Beraki, M. McDougal, M. L. Reese, Loss of a conserved MAPK causes catastrophic failure in assembly of a specialized cilium-like structure in *Toxoplasma gondii*. *Mol. Biol. Cell* **31**, 881–888 (2020).
18. M. K. Abe *et al*., ERK7 is an autoactivated member of the MAPK family. *J. Biol. Chem.* **276**, 21272–21279 (2001).
19. A. L. Chen *et al*., Novel insights into the composition and function of the *Toxoplasma* IMC sutures. *Cell. Microbiol.* **19**, cmi.12678 (2017).
20. K. Nishimura, T. Fukagawa, H. Takisawa, T. Kakimoto, M. Kanemaki, An auxin-based degron system for the rapid depletion of proteins in nonplant cells. *Nat. Methods* **6**, 917–922 (2009).
21. K. M. Brown, S. Long, L. D. Sibley, Plasma membrane association by N-acylation governs PKG function in *Toxoplasma gondii*. *MBio* **8**, e00375-17 (2017).
22. B. F. C. Kafsack *et al*., Rapid membrane disruption by a perforin-like protein facilitates parasite exit from host cells. *Science* **323**, 530–533 (2009).
23. V. B. Carruthers, L. D. Sibley, Mobilization of intracellular calcium stimulates microneme discharge in *Toxoplasma gondii*. *Mol. Microbiol.* **31**, 421–428 (1999).
24. P. Sharma, C. E. Chitnis, Key molecular events during host cell invasion by apicomplexan pathogens. *Curr. Opin. Microbiol.* **16**, 432–437 (2013).
25. N. J. Katris *et al*., The apical complex provides a regulated gateway for secretion of invasion factors in *Toxoplasma*. *PLoS Pathog.* **10**, e1004074 (2014).
26. E. Nagayasu, Y.-C. Hwang, J. Liu, J. M. Murray, K. Hu, Loss of a doublecortin (DCX)-domain protein causes structural defects in a tubulin-based organelle of *Toxoplasma gondii* and impairs host-cell invasion. *Mol. Biol. Cell* **28**, 411–428 (2017).
27. S. Long *et al*., Calmodulin-like proteins localized to the conoid regulate motility and cell invasion by *Toxoplasma gondii*. *PLoS Pathog.* **13**, e1006379 (2017).
28. S. Long, B. Anthony, L. L. Drewry, L. D. Sibley, A conserved ankyrin repeat-containing protein regulates conoid stability, motility and cell invasion in *Toxoplasma gondii*. *Nat. Commun.* **8**, 2236 (2017).
29. K. Hu *et al*., Cytoskeletal components of an invasion machine—The apical complex of *Toxoplasma gondii*. *PLoS Pathog.* **2**, e13 (2006).
30. S. Li, X. Prasanna, V. T. Salo, I. Vattulainen, E. Ikonen, An efficient auxin-inducible degron system with low basal degradation in human cells. *Nat. Methods* **16**, 866–869 (2019).
31. K. M. Sathyan *et al*., An improved auxin-inducible degron system preserves native protein levels and enables rapid and specific protein depletion. *Genes Dev.* **33**, 1441–1455 (2019).
32. K. J. Roux, D. I. Kim, B. Burke, BioID: A screen for protein-protein interactions. *Curr. Protoc. Protein Sci.* **74**, 19.23.1-19.23.14 (2013).
33. O. Söderberg *et al*., Direct observation of individual endogenous protein complexes in situ by proximity ligation. *Nat. Methods* **3**, 995–1000 (2006).
34. M. K. Abe *et al*., ERK8, a new member of the mitogen-activated protein kinase family. *J. Biol. Chem.* **277**, 16733–16743 (2002).
35. D. Sang *et al*., Ancestral reconstruction reveals mechanisms of ERK regulatory evolution. *eLife* **8**, e38805 (2019).
36. T. Tanoue, M. Adachi, T. Moriguchi, E. Nishida, A conserved docking motif in MAP kinases common to substrates, activators and regulators. *Nat. Cell Biol.* **2**, 110–116 (2000).
37. W. Peti, R. Page, Molecular basis of MAP kinase regulation. *Protein Sci.* **22**, 1698–1710 (2013).
38. H. Enslen, R. J. Davis, Regulation of MAP kinases by docking domains. *Biol. Cell* **93**, 5–14 (2001).
39. Á. Garai *et al*., Specificity of linear motifs that bind to a common mitogen-activated protein kinase docking groove. *Sci. Signal.* **5**, ra74 (2012).
40. M. Treeck, J. L. Sanders, J. E. Elias, J. C. Boothroyd, The phosphoproteomes of *Plasmodium falciparum* and *Toxoplasma gondii* reveal unusual adaptations within and beyond the parasites' boundaries. *Cell Host Microbe* **10**, 410–419 (2011).
41. P. D. Mace *et al*., Structure of ERK2 bound to PEA-15 reveals a mechanism for rapid release of activated MAPK. *Nat. Commun.* **4**, 1681 (2013).
42. C. I. Chang, B. E. Xu, R. Akella, M. H. Cobb, E. J. Goldsmith, Crystal structures of MAP kinase p38 complexed to the docking sites on its nuclear substrate MEF2A and activator MKK3b. *Mol. Cell* **9**, 1241–1249 (2002).
43. G. Gógl, I. Törő, A. Reményi, Protein-peptide complex crystallization: A case study on the ERK2 mitogen-activated protein kinase. *Acta Crystallogr. D Biol. Crystallogr.* **69**, 486–489 (2013).
44. E. Pellegrini *et al*., Structural basis for the subversion of MAP kinase signaling by an intrinsically disordered parasite secreted agonist. *Structure* **25**, 16–26 (2017).
45. P. Nioche *et al*., Crystal structures of the SH2 domain of Grb2: Highlight on the binding of a new high-affinity inhibitor. *J. Mol. Biol.* **315**, 1167–1177 (2002).
46. K. Ogura *et al*., Solution structure of the SH2 domain of Grb2 complexed with the Shc-derived phosphotyrosine-containing peptide. *J. Mol. Biol.* **289**, 439–445 (1999).
47. J. Hu, S. R. Hubbard, Structural characterization of a novel Cbl phosphotyrosine recognition motif in the APS family of adapter proteins. *J. Biol. Chem.* **280**, 18943–18949 (2005).
48. A. J. Bardwell, M. Abdollahi, L. Bardwell, Docking sites on mitogen-activated protein kinase (MAPK) kinases, MAPK phosphatases and the Elk-1 transcription factor compete for MAPK binding and are crucial for enzymic activity. *Biochem. J.* **370**, 1077–1085 (2003).
49. C. A. Taylor IV *et al*., Functional divergence caused by mutations in an energetic hotspot in ERK2. *Proc. Natl. Acad. Sci. U.S.A.* **116**, 15514–15523 (2019).
50. S. H. Yang, P. R. Yates, A. J. Whitmarsh, R. J. Davis, A. D. Sharrocks, The Elk-1 ETS-domain transcription factor contains a mitogen-activated protein kinase targeting motif. *Mol. Cell. Biol.* **18**, 710–720 (1998).
51. G. Manning, D. B. Whyte, R. Martinez, T. Hunter, S. Sudarsanam, The protein kinase complement of the human genome. *Science* **298**, 1912–1934 (2002).
52. C. J. Sherr, J. M. Roberts, CDK inhibitors: Positive and negative regulators of G1-phase progression. *Genes Dev.* **13**, 1501–1512 (1999).
53. A. A. Russo, P. D. Jeffrey, A. K. Patten, J. Massagué, N. P. Pavletich, Crystal structure of the p27Kip1 cyclin-dependent-kinase inhibitor bound to the cyclin A-Cdk2 complex. *Nature* **382**, 325–331 (1996).
54. M. Pagano *et al*., Role of the ubiquitin-proteasome pathway in regulating abundance of the cyclin-dependent kinase inhibitor p27. *Science* **269**, 682–685 (1995).
55. F. Sievers *et al*., Fast, scalable generation of high-quality protein multiple sequence alignments using Clustal Omega. *Mol. Syst. Biol.* **7**, 539 (2011).
56. G. E. Crooks, G. Hon, J.-M. Chandonia, S. E. Brenner, WebLogo: A sequence logo generator. *Genome Res.* **14**, 1188–1190 (2004).
57. P. Bastin, Z. Bagherzadeh, K. R. Matthews, K. Gull, A novel epitope tag system to study protein targeting and organelle biogenesis in *Trypanosoma brucei*. *Mol. Biochem. Parasitol.* **77**, 235–239 (1996).
58. G. I. Evan, G. K. Lewis, G. Ramsay, J. M. Bishop, Isolation of monoclonal antibodies specific for human c-myc proto-oncogene product. *Mol. Cell. Biol.* **5**, 3610–3616 (1985).
59. J. L. Burg, D. Perelman, L. H. Kasper, P. L. Ware, J. C. Boothroyd, Molecular analysis of the gene encoding the major surface antigen of *Toxoplasma gondii*. *J. Immunol.* **141**, 3584–3591 (1988).
60. J. R. Beck *et al*., A *Toxoplasma* palmitoyl acyl transferase and the palmitoylated Armadillo repeat protein TgARO govern apical rhoptry tethering and reveal a critical role for the rhoptries in host cell invasion but not egress. *PLoS Pathog.* **9**, e1003162 (2013).

61. S. M. Nadipuram *et al*., In vivo biotinylation of the *Toxoplasma* parasitophorous vacuole reveals novel dense granule proteins important for parasite growth and pathogenesis. *MBio* **7**, e00808-16 (2016).
62. M. J. Wichroski, J. A. Melton, C. G. Donahue, R. K. Tweten, G. E. Ward, *Clostridium septicum* alpha-toxin is active against the parasitic protozoan *Toxoplasma gondii* and targets members of the SAG family of glycosylphosphatidylinositol-anchored surface proteins. *Infect. Immun.* **70**, 4353–4361 (2002).
63. T. Beraki *et al*., Divergent kinase regulates membrane ultrastructure of the *Toxoplasma* parasitophorous vacuole. *Proc. Natl. Acad. Sci. U.S.A.* **116**, 6361–6370 (2019).
64. T. Endo, K. Yagita, Effect of extracellular ions on motility and cell entry in *Toxoplasma gondii*. *J. Protozool.* **37**, 133–138 (1990).
65. C. P. Choi *et al*., A photoactivatable crosslinking system reveals protein interactions in the *Toxoplasma gondii* inner membrane complex. *PLoS Biol.* **17**, e3000475 (2019).
66. P. Kaiser, J. Wohlschlegel, Identification of ubiquitination sites and determination of ubiquitin-chain architectures by mass spectrometry. *Methods Enzymol.* **399**, 266–277 (2005).
67. J. A. Wohlschlegel, Identification of SUMO-conjugated proteins and their SUMO attachment sites using proteomic mass spectrometry. *Methods Mol. Biol.* **497**, 33–49 (2009).
68. A. Michalski *et al*., Mass spectrometry-based proteomics using Q Exactive, a high-performance benchtop quadrupole Orbitrap mass spectrometer. *Mol. Cell. Proteomics* **10**, M111.011015 (2011).
69. C. D. Kelstrup, C. Young, R. Lavallee, M. L. Nielsen, J. V. Olsen, Optimized fast and sensitive acquisition methods for shotgun proteomics on a quadrupole Orbitrap mass spectrometer. *J. Proteome Res.* **11**, 3487–3497 (2012).
70. D. L. Tabb, W. H. McDonald, J. R. Yates III, DTASelect and contrast: Tools for assembling and comparing protein identifications from shotgun proteomics. *J. Proteome Res.* **1**, 21–26 (2002).
71. T. Xu *et al*., ProLuCID: An improved SEQUEST-like algorithm with enhanced sensitivity and specificity. *J. Proteomics* **129**, 16–24 (2015).
72. D. Cociorva, D. L. Tabb, J. R. Yates, Validation of tandem mass spectrometry database search results using DTASelect. *Curr. Protoc. Bioinformatics*, chap. 13, unit 13.4 (2007).
73. L. Florens *et al*., Analyzing chromatin remodeling complexes using shotgun proteomics and normalized spectral abundance factors. *Methods* **40**, 303–311 (2006).
74. A. Sali, T. L. Blundell, Comparative protein modelling by satisfaction of spatial restraints. *J. Mol. Biol.* **234**, 779–815 (1993).
75. A. J. McCoy *et al*., Phaser crystallographic software. *J. Appl. Crystallogr.* **40**, 658–674 (2007).
76. P. Emsley, B. Lohkamp, W. G. Scott, K. Cowtan, Features and development of Coot. *Acta Crystallogr. D Biol. Crystallogr.* **66**, 486–501 (2010).
77. P. D. Adams *et al*., PHENIX: A comprehensive Python-based system for macromolecular structure solution. *Acta Crystallogr. D Biol. Crystallogr.* **66**, 213–221 (2010).
78. V. B. Chen *et al*., MolProbity: All-atom structure validation for macromolecular crystallography. *Acta Crystallogr. D Biol. Crystallogr.* **66**, 12–21 (2010).
79. J. Schindelin *et al*., Fiji: An open-source platform for biological-image analysis. *Nat. Methods* **9**, 676–682 (2012).